Marine Geology
March 2023, Volume 457 Pages 107004 (11p.)
https://doi.org/10.1016/j.margeo.2023.107004
https://archimer.ifremer.fr/doc/00820/93189/

Deep-water circulation intensity and stratification in the South China Sea since the last glaciation

Zhao Yulong [1?*], Wang Yuwei [1], Liu Zhifei [1], Li Xiajing [1], Yang Wenguang [2]

[1] State Key Laboratory of Marine Geology, Tongji University, Shanghai 200092, China
[2] Institute of Sedimentary Geology, Chengdu University of Technology, Chengdu 610059, China

* Corresponding author : Yulong Zhao, email address : yeoloon@tongji.edu.cn

Abstract :

Deep-water circulation in the South China Sea is closely linked to deep hydrography of the North Pacific via water exchange at the Luzon Strait. In this study, temporal changes of the paleocurrent intensity in the South China Sea are established using the detrital sortable silt proxy to reconstruct the evolution of deep hydrography of the subarctic Pacific since the last deglaciation. The results show that deep (>1500 m) currents in the South China Sea were relatively vigorous during the last glacial period, and relatively weak during the Holocene. A gradual decrease of current speed during the last deglaciation was observed at both ~1650 m and ~ 2000 m water depths. Furthermore, the current-intensity decline started earlier in relatively shallow portion (~1650 m) than in deep portion (~2000 m). This disparity is interpreted to be associated with the gradual deepening of the glacial North Pacific Intermediate Water, which reduced the pressure gradients between the Pacific and the South China Sea at the depth levels it affected. Such processes also greatly altered the stratification in the South China Sea: a strong stratification existed prior to the Heinrich Stadial 1, but it vanished owing to the enhanced vertical mixing brought by downward penetration of the glacial North Pacific Intermediate Water. Our study provides new insights into the evolution of deep hydrography in the subarctic Pacific, and the processes how such changes affect the subtropical Pacific under glacial boundary condition.

Highlights

► Slowdown of SCS deep circulation in response to intrusion of the glacial NPIW. ► Gradual deepward extending of the glacial NPIW in the subtropical Pacific. ► Strong glacial stratification in the deep SCS vanished at onset of the H-1 Event.

Keywords : paleocurrent intensity, sortable silt, deep circulation, stratification, glacial North Pacific Intermediate Water, South China Sea

1. Introduction

Hydrography of the deep North Pacific (> 1500 m) has been the focus of many paleoceanographic studies over the last decades as it plays a crucial role in driving global climate change and carbon cycles (Galbraith et al., 2007; Gray et al., 2018). Although numerous studies have been performed, the variation of intermediate and deep circulation at high-latitude North Pacific under glacial condition and its influence on deep circulation of the subtropical Pacific are still under debates (Keigwin, 1998; Matsumoto et al., 2002; Ohkushi et al., 2003; Broecker et al. 2008; Herguera et al., 2010; Horikawa et al., 2010; Okazaki et al, 2010; Rella et al., 2012; Jaccard and Galbraith, 2013). The South China Sea, the largest marginal basins of the western Pacific, provides an ideal venue to gain insights into the past changes of deep hydrography of the North Pacific, because of its (1) active deep-water exchange with the Pacific both at present time (Li and Qu, 2006; Wu et al., 2015) and during the last glacial period (Wan and Jian, 2014; Wan et al., 2018); and (2) high sedimentation rate and good preservation of carbonates relative to the open Pacific Ocean (Liu et al., 2009).

Under the present-day condition, deep-water (>1500 m) circulation in the South China Sea is predominantly driven by water exchange with the Pacific Ocean via the Luzon Strait, the sole deep-water renewal channel of the South China Sea (Qu et al., 2006; Lan et al., 2013). As deep water at the Pacific side is denser than the South China Sea side, North Pacific Deep Water (NPDW) enters the South China Sea via the Luzon Strait under influences of the baroclinic pressure gradient (Qu et al., 2006). Owing to dissipation of the high potential vorticity brought by intrusion of the NPDW, a cyclonic deep circulation is formed in the South China Sea (Lan et al., 2013; Zhu et al., 2017). According to the abyssal circulation theory, intensity of such deep circulation in the South China Sea is positively proportional to the volume transport of deep-water overflow through the Luzon Strait (Lan et al., 2013). Therefore, considering that topography of the Luzon Strait kept stable during the last glacial cycles, variations of the South China Sea deep current intensity reflect changes of the variability of volume transport of deep-water inflow from the Pacific, which is further decided by the density gradient between two sides of the Luzon Strait.

During the last glacial period, especially the Heinrich Stadial 1 (H-1, ~17.5–14.6 ka), deep circulation in the South China Sea was greatly altered following changes of deep hydrography in the North Pacific (Zheng et al., 2016). Under the glacial boundary condition, mid-depth circulation of the North Pacific was strengthened by formation of the glacial North Pacific Intermediate Water (NPIW) in the subarctic Pacific (Matsumoto et al., 2002; Okazaki et al., 2012), and the NPDW was extended to a depth range of ~2500–3000 m (Okazaki et al., 2010; Menviel et al., 2011). Due to enhanced convection of the glacial NPIW to the subtropical Pacific (Max et al., 2017), the glacial NPIW became the most prominent source of deep water in the South China Sea since the last glacial maximum (LGM, 18–24 ka) (Wan and Jian, 2014;

Wan et al., 2018). Relative to the NPDW, the glacial NPIW was higher in temperature and lower in salinity, and thus lighter in density, which would reduce the pressure gradient between two sides of the Luzon Strait and induce slowdown of the deep circulation in the South China Sea.

As a sedimentological manifestation of the deep circulation, a sequence of contourite drifts are developed along the northern border of the South China Sea (Shao et al., 2007; Yin et al., 2019). Among all those contourite drifts, the elongated drift at southeast off Dongsha Islands has drawn the attentions of many paleoceanographers owing to its extreme high accumulation rate (>100 cm/kyr for the last 40 kyr, Shao et al., 2007). Sediment cores taken from this contourite drift has yielded valuable information on the high-resolution variability of paleoclimatic and paleoceanographic conditions over the last and penultimate glacial cycles (Wang et al., 1999; Tamburini et al., 2003; Wei et al., 2004; Hu et al., 2012). These sediment cores also afford records of paleocurrent intensity change in the deep South China Sea at relatively high temporal resolution.

In the present study, grain size analyses of terrigenous particles were performed on two sediments cores (Core MD05-2903 and ODP Site 1144) respectively from ~1650 and 2000 m water depths of the elongated drift at southeast off Dongsha Islands in the northern South China Sea. Paleocurrent intensity of the deep South China Sea circulation was reconstructed using the 'sortable silt' proxy. The 'sortable silt' (10–63 μm) denotes the portion of detrital sediments that is not strongly affected by cohesive behavior of the clayey sediments, and it has been proposed that mean grain size ($\overline{SS}$) and percentage (SS%) of sortable silts vary sensitively with flow speed of the depositing currents (McCave et al., 1995). Recent laboratory experiment results indicate that, at a particular location in the flume, $\overline{SS}$ was linearly related to current speeds, bearing out the robustness of the 'sortable silt' paleocurrent proxy (Culp et al., 2021). The 'sortable silt'

proxy has been widely used to reconstruct changes of paleocurrent intensities over various basins of the world ocean (see examples in McCave and Hall, 2006). The scientific objectives of this study include (1) reconstructing evolution of the deep circulation of the South China Sea since the last glacial period, (2) investigating the temporal changes of stratification condition in the deep South China Sea, and (3) evaluating the potential influences of deep hydrographic changes in the North Pacific, especially development of the glacial NPIW during the H-1 cold event, on the deep circulation of the South China Sea.

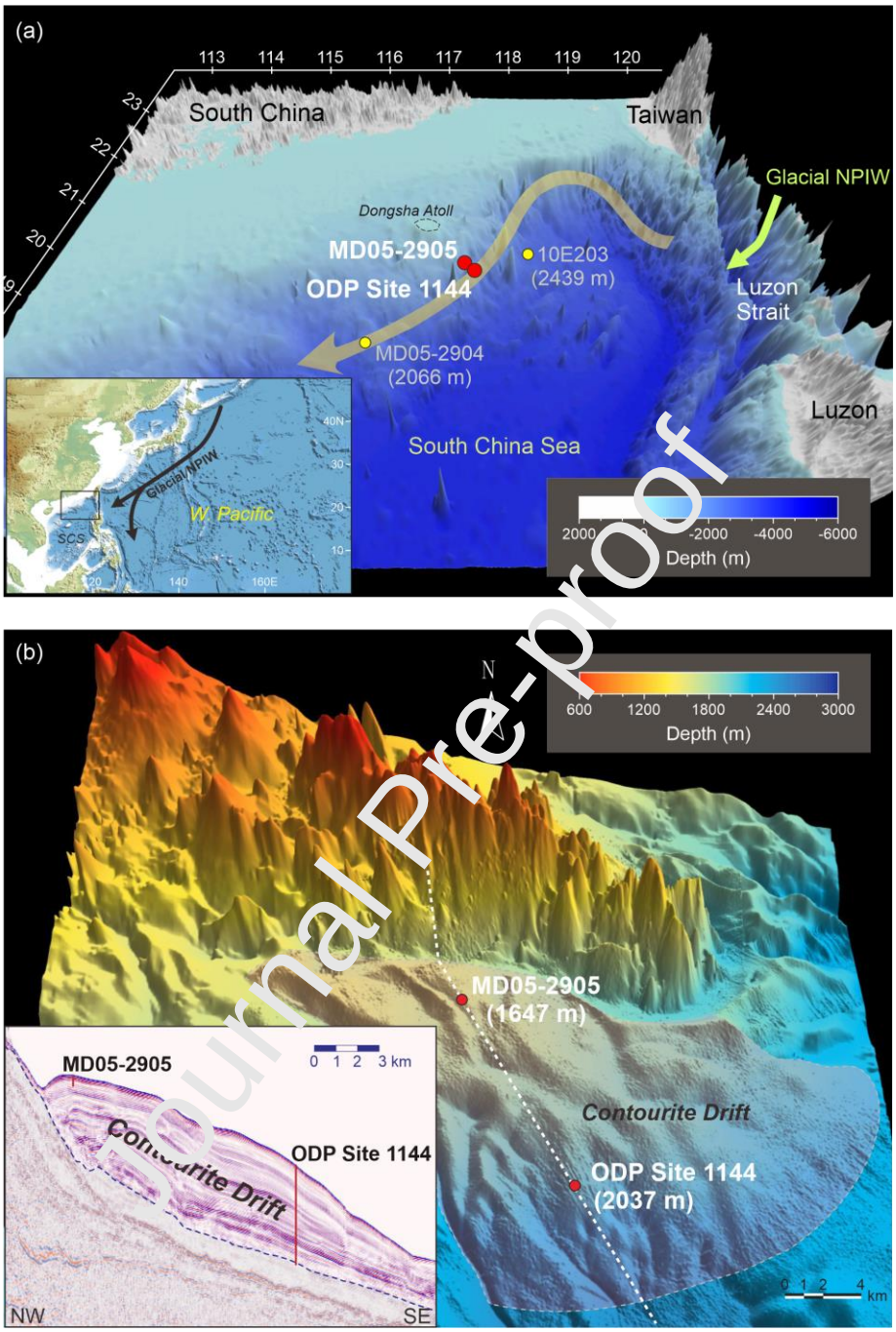

Figure 1. (a) Map showing the locations of Core MD05-2905 and ODP Site 1144. The yellow arrowed curve indicates the approximate pathway of deep currents in the northern South China Sea. The olivine curve indicates the intrusion of the glacial NPIW into the South China Sea during the last deglaciation. The map at the left bottom corner shows the location of the studied regions in the western Pacific. (b) Enlarged three-dimensional bathymetric map showing the locations of Core MD05-2905 and ODP Site 1144 on the contourite drift at southeast off Dongsha Atoll. The white dashed line shows position of the seismic profile of the contourite drift in the left lower panel (Yin et al., 2019).

2. Materials and Methods

Two sediment cores, Core MD05-2905 and Ocean Drilling Program (ODP) Site 1144, respectively collected on the upper and middle parts of the contourite drift at southeast off Dongsha Islands, were chosen to perform grain-size analyses of detrital particles (Figure 1). Core MD05-2905 (20°8.17′N, 117°21.61′E, water depth ~1647 m) was obtained from the upper portion of the elongated drift during the 'MD147/Marco Polo-IMAGES XII' cruise of R/V Marion Dufresne (Laj et al., 2005). A total number of 120 samples were obtained from Core MD05-2905 at a depth resolution of 4 cm. ODP Site 1144 (20°3.18′N, 117°25.14′E, water depth ~2037 m) was obtained from the middle portion of the same contourite drift during ODP Leg 184 (Wang et al., 2000). In total, 158 samples were collected from the topmost 31.5 m of ODP Site 1144 at a depth resolution of 20 cm per sample.

Chronology of Core MD05-2905 and ODP Site 1144 were established respectively based on 12 and 7 accelerator mass spectrometry (AMS) ^{14}C dating points of planktonic foraminifera (*Globigerinoides ruber*, *Globigerinoides sacculifer* or mixed planktonic foraminifers) (Table 1; Bühring et al., 2004; Yang, 2008). To obtain the calendar ages of AMS ^{14}C dating points, the conventional radiocarbon ages were recalibrated by the program Calib 8.1.0 (Stuiver and Reimer, 1993), using the Marine20 calibration dataset (Heaton et al., 2020) and a ΔR value of -87±48 (regional mean of the South China Sea) (Southon et al., 2002; Yoneda et al., 2007). According to the chronology of Core MD05-2905, the total 11.98 m sediments covered a time interval of ~2.4–27.6 ka, with an average sedimentation rate of ~47.6 cm/kyr. The topmost 31.5 m of ODP Site 1144 covered a time span of the last ~27.9 ka, with an average sedimentation rate of ~113 cm/kyr. Linear sedimentation rates (LSR) of the two cores were roughly at the same

level during the Holocene, while LSR of ODP Site 1144 were around 2–4 times higher than Core MD05-2905 during the last glacial period (Figure 2).

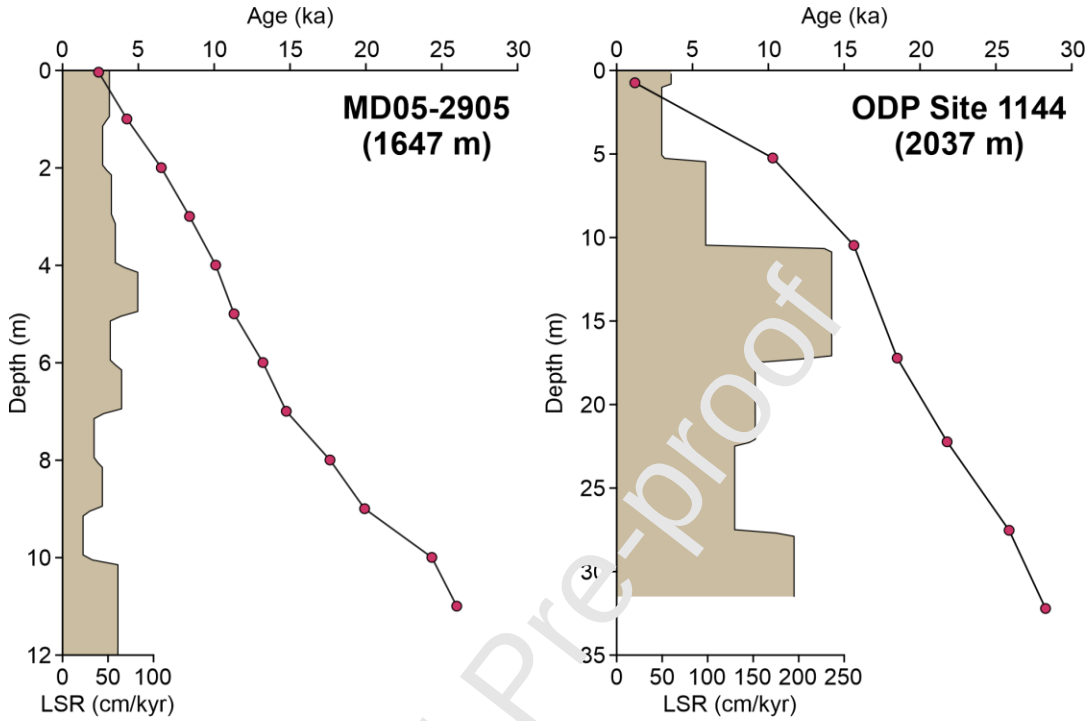

Figure 2. Depth-age plots and linear sedimentation rates (LSR) of Core MD05-2905 and ODP Site 1144. The magenta solid circles show the AMS ^{14}C dating points (Bühring et al., 2004; Yang, 2008).

Grain-size analyses of detrital sediments were performed on the fine detrital sediments (<63 μm) using a Micromeritics SediGraphIII Plus 5120 Particle Size Analyzer in State Key Laboratory of Marine Geology, Tongji University. By measuring the rate at which particles fall under gravity through a liquid having known properties, the SediGraph can determine the equivalent spherical diameter of particles according to the Stokes' Law of Particle Settling. Relative to the widely-used laser diffraction grain-size analytical method, the SediGraph technique can better indicate the dynamics of sediment deposition, thus is the optimum instrument for paleocurrent reconstruction (Bianchi et al., 1999; McCave et al., 2006).

Table 1. AMS ^{14}C dating points for Core MD05-2905 (Yang, 2008) and ODP Site 1144 (Bühring et al., 2004)

Core	Depth (cm)	Dating materials	Conventional age (^{14}C yr BP, 1σ)	Calibrated age (cal yr BP)	Calibrated age range (cal yr BP, 1σ)
MD05-2905	3.5	*G. ruber & G. sacculifer*	2723±42	2380	2272–2499
MD05-2905	99.5	*G. ruber*	4222±25	4243	4140–4353
MD05-2905	199.5	*G. ruber*	6182±28	6510	6412–6605
MD05-2905	299.5	*G. ruber*	7987±38	8372	8281–8465
MD05-2905	399.5	*G. ruber & G. sacculifer*	9344±35	10097	9999–10209
MD05-2905	499.5	*G. ruber*	10235±33	11306	11187–11396
MD05-2905	599.5	*G. ruber*	11805±37	13212	13120–13295
MD05-2905	699.5	*G. ruber*	12923±39	14752	14589–14920
MD05-2905	799.5	*G. ruber*	15152±42	17632	17474–17784
MD05-2905	899.5	*G. ruber*	17150±48	19916	19777–20073
MD05-2905	999.5	*G. ruber*	21007±61	24347	24187–24503
MD05-2905	1099.5	*G. ruber & G. sacculifer*	22555±101	25989	25835–26129
ODP Site 1144	73.5	mixed planktonic foraminifers	1721±60	1201	1105–1296
ODP Site 1144	524	mixed bulk planktonic foraminifers	9487±65	10289	10168–10410
ODP Site 1144	1047	mixed planktonic foraminifers	13571±75	15637	15476–15799
ODP	1722	*G. ruber & G.*	15930±80	18494	18340–18642

Site 1144		*sacculifer*			
ODP Site 1144	2223	*G. ruber & G. sacculifer*	18650±90	21785	21618–21979
ODP Site 1144	2753	mixed planktonic foraminifers	22430±110	25872	25726–25996
ODP Site 1144	3221	*G. ruber & G. sacculifer*	24860±160	28273	28047–28517

Before measured on the SediGraph, the marine sediment samples were pretreated following the procedures described in Bianchi et al (1999). Subsamples of ~3.0 g of raw sediments were firstly wet sieved using a 250-mesh stainless-steel sieve to remove particles greater than 63 μm. The residues were treated successively with 3% (~1 mol/L) hydrogen peroxide (H_2O_2) and 1 mol/L hydrogen chloride (HCl) solutions to eliminate biogenic organic matter and carbonates. Inspection of representative samples under a binocular microscope showed that biogenic silica was negligible in the <63 μm fraction and removal of this component was therefore not necessary. The mixtures were then rinsed several times using deionized water to remove residues of H_2O_2 and HCl, until pH of the solutions became ~7. The suspensions were then dispersed into 120 ml of 0.1 mol/L sodium hexametaphosphate [$(NaPO_3)_6$] solution to avoid aggregation of fine fractions. Given that total percentage of the carbonate and organic components in both ODP Site 1144 and Core MD05-2905 varied in the range of 10–20% (Wei et al., 2004; Kienast et al., 2005; Yang, 2008) and the >63 μm fraction was negligible (Yang, 2008), the <63 μm fine detrital fraction accounted for ~2.4–2.7 g in the ~3.0 g of raw sediments. It gave a sample concentration of 20–22.5 g/L (≈2% by volume), which was necessary to avoid hindered settling of particles (Coakley and Syvitski, 1991; Bianchi et al., 1999). The suspensions were then poured into the sample dispersion unit of the SediGraph Particle Size Analyzer to perform grain-size analyses.

The measurement range was set to 0.2–63 μm, and it took ~70 min for each sample to be analyzed. The SS% was calculated as the subtotal sum of percentages of all grain-size grades in the range of 10-63 μm. The $\overline{SS}$ is calculated as the arithmetic mean of log-transformed volume frequency size of the 10–63 μm range (McCave et al., 2017) using the equations below:

$$\overline{SS} = \frac{\sum \phi_i P_i}{\sum P_i} \quad (1)$$

$$\phi_i = -\log_2 D_i \ \ (D_i \in [10, 63] \ \mu m) \quad (2)$$

where $D_i \in [10, 63]$ μm is the grain-size grades of sortable silts, ϕ_i is the phi scale of each grain-size grade, and P_i is the percentage of grains in each corresponding grain-size grade. The $\overline{SS}$ calculated using Equation (1) was in the phi scale, and it was then converted back to microns using the reciprocal equation of (2).

3. Results

The fine detrital sediments of Core MD05-2905 are composed mainly of clayey (<4 μm) sediments, with moderate proportion of sortable silts (10–63 μm) and relatively low cohesive silts (4–10 μm) (Figure 3). The clayey and sortable silt fractions respectively represent 43–68% (average ~56%) and 11–38% (average ~24%) of the fine detrital sediments, with cohesive silts in the range of 16–25% (average ~20%). Median grain sizes of the detrital sediments (<63 μm) of Core MD05-2905 vary in the range of 1.9–5.5 μm. Temporal variations of clayey and sortable silt contents, as well as the median grain size, are subdivided into a three-stage evolution since ~27.6 ka. During the first stage (27.6–18.9 ka), grain-size variations are characterized by relatively low clayey proportions (43–52%, average 48%), high sortable silts (30–38%, average ~35%), and elevated median grain size (4.0–5.5 μm, average 4.6 μm). During the last deglaciation (the second stage, 18.9–10.7 ka), a clear increasing tendency of clayey fraction

(from 47% to 69%), along with a decrease of sortable silt contents from 37% to 11%, is observed. The median grain size values are also decreased from ~4.0 μm to 2.5 μm during the second stage. Relatively high abundance of clayey sediments (57–69%, average ~62%) and low abundance of sortable silts (~11–19%, average ~14%), as well as low values of median grain size (1.9–3.1 μm, average 2.6 μm), are observed in the Holocene (the third stage, 10.7–2.4 ka). Similar to the variations of SS%, the $\overline{SS}$ of MD05-2905 has also undergone a three-stage temporal changes since ~27.6 ka: relatively high (18.2–20.2 μm, average 19.0 μm) during the first stage (27.6–18.9 ka) and low in the Holocene (~15.0–17.4 μm, average 16.2 μm), with a decreasing trend observed during the last deglaciation (Figure 3).

Detrital sediments of ODP Site 1144 are also dominated by clayey sediments, with relatively low proportions of sortable silts and cohesive silts (Figure 3). The clayey fraction accounts for ~50–77% (average ~61%) of the fine detrital sediments, with sortable silts vary in the range of 7–29% (average ~20%). Comparing to the clayey and sortable silt fractions, variability of the cohesive silt contents is relatively low (15–23%, average 19%). Median grain sizes of ODP Site 1144 vary between 1.2 μm and 3.9 μm, with an average value of 2.6 μm. Akin to temporal variations of grain sizes in Core MD05-2905, clayey and sortable silt contents, and the median grain size of ODP Site 1144 can also be subdivided into a three-stage evolution since ~27.9 ka. During the first stage (27.9–17.1 ka), grain-size variations are featured by less abundant clayey fraction (50–63%, average 56%), elevated sortable silt contents (20–28%, average ~24%), and relatively high values of median grain size (2.2–3.9 μm, average ~3.1 μm). An increase of clayey fraction from 54% to 77%, as well as decreases of sortable silt contents (from 27% to 7%) and median grain sizes (from 2.8 μm to 1.2 μm), are observed during the second stage (17.1–10.9 ka). During the Holocene (the third stage, after 10.9 ka), clayey

sediments (64–75%, average ~69%) are highly abundant in ODP Site 1144, with relatively low abundance of sortable silts (~9–17%, average ~13%) and low values of median grain size (1.4–2.2 μm, average 1.8 μm) observed. The $\overline{SS}$ values of ODP Site 1144 are slightly higher during the first stage (~15.8–18.4 μm, average 17.2 μm) than in the Holocene (~15.1–17.0 μm, average 16.1 μm), with a subtle decreasing trend observed during the last deglaciation (Figure 3). Two peaks of $\overline{SS}$ are observed during the last deglaciation, with the first centered at ~16.9 ka, and the second centered at ~13.3 ka (Figure 3).

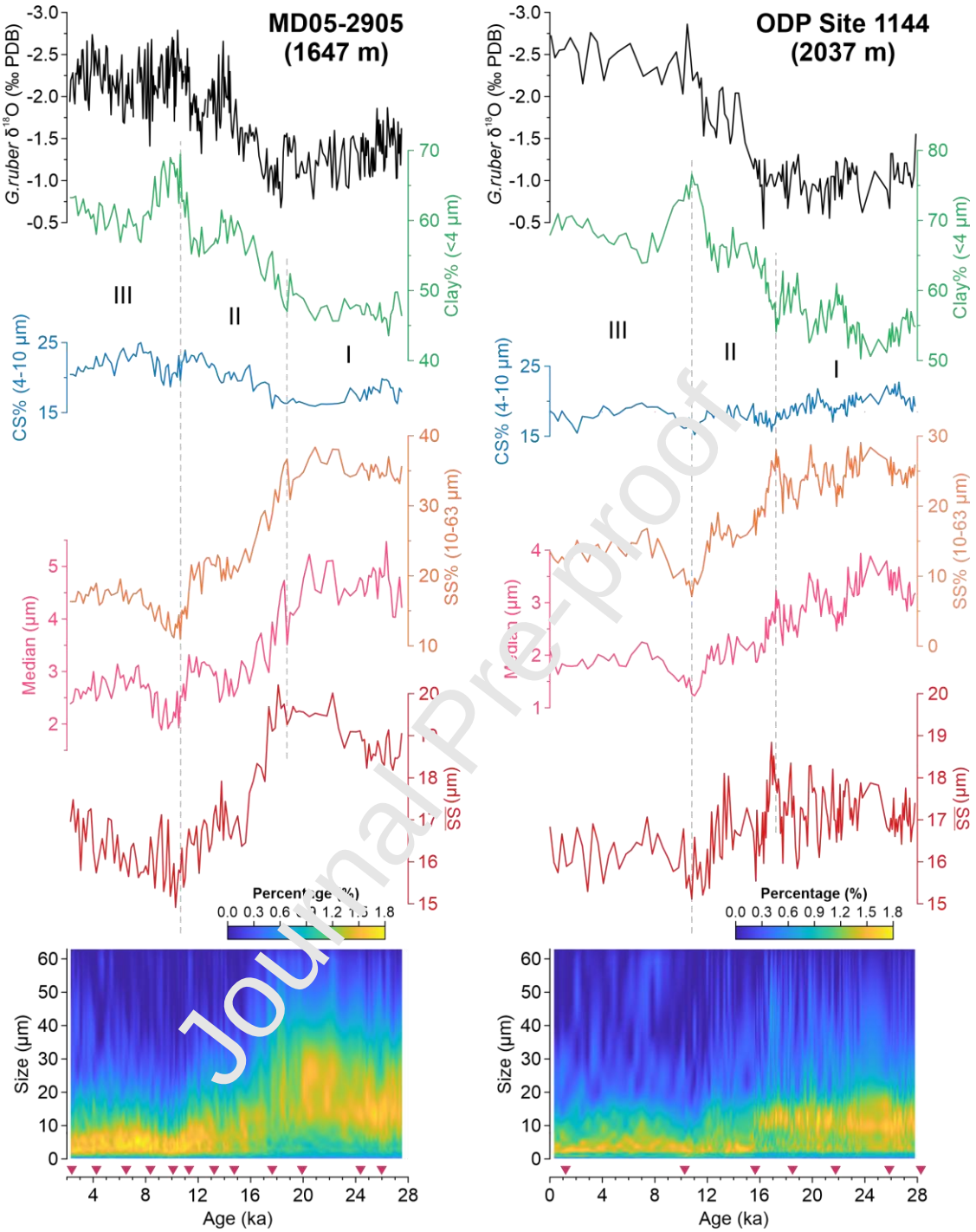

Figure 3. Temporal changes of the contents of clay, cohesive silts (CS) and sortable silts (SS), median grain size and sortable silt mean grain size ($\overline{SS}$) of Core MD05-2905 and ODP Site 1144. The pseudo-color plots show the changes in grain-size frequency distribution of particles <63 μm. $\delta^{18}O$ stratigraphy of planktonic foraminifera *Globigerinoides ruber* and the radiocarbon dating points (the inverted triangular marks in magenta) of Core MD05-2905 and ODP Site 1144 are from Yang (2008) and Bühring et al (2004), respectively. The Roman numerals indicate the three stages of grain-size evolution in each core.

4. Discussions

4.1. Validation of sortable silt proxies as indicators of paleo-current intensities

The mean grain size ($\overline{SS}$) and percentage (SS%) of sortable silts are highly sensitive to hydrodynamics of the deep-sea currents from which the sediments are deposited, and thus are widely used as indicators of paleocurrent intensity changes over various basins of the world ocean (McCave and Hall, 2006). However, the robustness of these proxies can be affected by extra input of coarse particles by downslope transport or vertical sinking from water column (McCave and Hall, 2006). For the low latitudes, vertical sinking detrital particles to the deep-sea environments mostly coming from aerosol dusts (Duce et al., 1991). According to the satellite-based and in-situ observational data, dust flux to the northern SCS is around 18 g/m^2/yr (Wang et al., 2012; Du et al., 2020). Taking the LSR of the topmost samples of ODP Site 1144 and Core MD05-2905 (~50–60 cm/kyr, Figure 2), and an average density of 2.5 g/cm^3 for the bulk sediments, we can roughly estimate that sediment flux to the contourite drift is around 1250–1500 g/m^2/yr under the present-day condition. It implies that aerosol dusts represent only <1.5% of sediment flux to the studied sites. The contourite drift where ODP Site 1144 and Core MD05-2905 are located is beneath a seamount, which is connected to the Dongsha Atoll (Figure 1). Downslope transport of detrital particles to the contourite drift is rare, if not none, because of the absence of stable sediment supply to the coral atoll. Therefore, the sortable silt fraction of ODP Site 1144 and Core MD05-2905 is hardly affected by either downslope transport or vertical sinking of particles. The $\overline{SS}$-SS% correlation coefficient is usually adopted to test the validity of the sortable silt proxy, as $\overline{SS}$ and SS% usually display a close relationship in a well current-sorted deposit (McCave et al., 1995, 2017; McCave and Hall, 2006; McCave and Andrews, 2019). The $\overline{SS}$ and SS% of both ODP Site 1144 and MD05-2905 are well correlated, with Reduced Major

Axis (RMA) correlation coefficients (r values) of ~0.74 and ~0.90 respectively (Figure 4). Accordingly, we propose that $\overline{SS}$ and SS% of ODP Site 1144 and Core MD05-2905 reflect mostly variability of paleo-current intensities in the deep South China Sea.

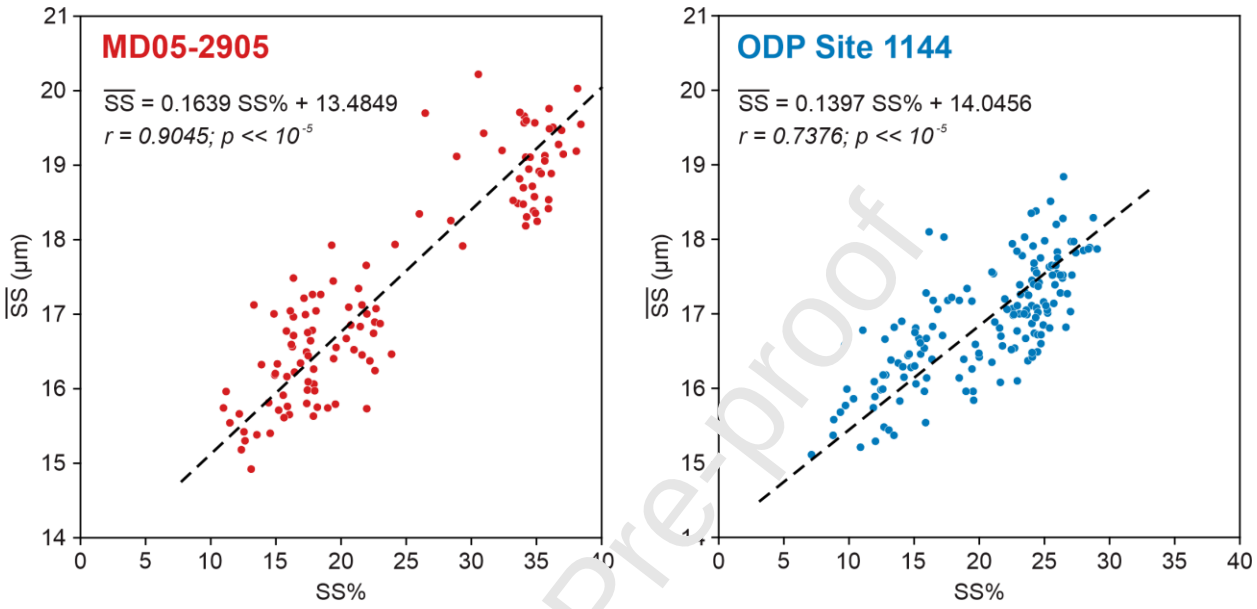

Figure 4. Plots of $\overline{SS}$ versus SS% for ODP Site 1144 and Core MD05-2905 show good correlation of the two proxies. The dashed lines and equations show the Reduced Major Axis (RMA) regressions of $\overline{SS}$ versus SS%, with *r* and *p* values indicate respectively the correlation coefficients and the null-hypothesis significance levels.

The South China Sea is characterized by a continental shelf as wide as ~200 km at its northern border. Over the last glacial cycle, the global sea level dropped >120 m (relative to the modern sea level) during 29–16.5 ka and rose rapidly to ~ 5 m below modern sea level during 16.5–7 ka (Lambeck et al., 2014). During low-stands of sea level in the last glacial cycles, the northern South China Sea continental shelf was largely emerged, leading to seaward migration of coastline and the major river mouths. Such changes in land-sea configuration facilitates the inputs of detrital sediments to the deep South China Sea (Sun et al., 2003). For the northeastern sector of South China Sea, where ODP Site 1144 and Core MD05-2905 are located, detrital sediments are mostly provided by riverine inputs from Taiwan and Luzon, with South China

(mostly Pearl River) plays a minor role (Liu et al., 2016). The continental shelves off Taiwan and Luzon are quite narrow relative to the northern border of the South China Sea, and thus sediment supply from these sources is not sensitive to sea-level changes during the late Quaternary glacial cycles. Fluvial sediments from Pearl River was brought westward by the strong coastal currents on the shelf and contour currents in the deep sea, and only <10% can reach the studied sites (Liu et al., 2010, 2016). As a result, input of detrital sediments, either clay minerals or magnetic particles, to the northern South China Sea are hardly affected by sea-level changes (Liu et al., 2016; Kissel et al., 2020). Rather, their variations in the late Quaternary glacial cycles reflect mostly changes in the intensity of bottom oceanic circulation (Kissel et al., 2020).

4.2. Variability of the South China Sea deep circulation since the last glacial period

Combining $\overline{SS}$ and SS% results of the two cores, we found that paleocurrent intensities in the northern South China Sea can also be subdivided into a three-stage evolution since ~28 ka: relatively strong currents during the last glacial period, a gradual decrease of current speeds during the last deglaciation, and relatively weak currents in the Holocene (Figure 5). In essence, intensity of deep currents in the South China Sea is forced by dissipation of the potential vorticity introduced by deep-water intrusion from the Pacific (Lan et al., 2013; Zhu et al., 2017). According to the area integral equation of potential vorticity in the South China Sea, intensity of the deep circulation is positively proportional to the volume transport, and inversely proportional to the layer thickness of the deep-water overflow through the Luzon Strait (Lan et al., 2013). As a result, possible mechanism for variability of the South China Sea deep circulation can be changes in volume transport and/or layer thickness of deep-water overflow through the Luzon Strait. The upper boundary of water inflow from the Pacific is 1500–1700 m in the modern South China Sea (Zhu et al., 2019), and such depth limit has remained almost unchanged since the

LGM (Li et al., 2018). As lower limit of the Pacific inflow is confined by the sill depth of the Luzon Strait (~2400 m), it implies that the layer thickness of deep-water inflow from the Pacific has been quasi-stable since the LGM. Therefore, variability of South China Sea deep circulation was mostly induced by changes of volume transport of deep-water overflow through the Luzon Strait, which is further driven by density gradient between two sides of the Luzon Strait (Qu et al., 2006; Zhu et al., 2017). As seawater density is mostly decided by its temperature and salinity, the gradual slowdown of the South China Sea deep circulation since the last glacial period thus indicates intrusion of warmer and/or less salty water from the Pacific.

By measuring radiocarbon ages of deep water, Wan and Jian (2014) inferred that the most prominent source of deep water in the South China Sea during the last deglaciation was the relatively young glacial NPIW newly formed in the subarctic Pacific (Figure 5g). As the glacial NPIW was warmer and less salty than the NPDW (Gong et al., 2019), slowdown of the SCS deep circulation during the last deglaciation probably reflects initiation of the glacial NPIW influences on the deep circulation in the South China Sea. Numeric modelling simulations indicated that the glacial NPIW formation in the subarctic Pacific was largely enhanced during the H-1, in response to the enhanced convection in the middle of Okhotsk and the western Bering Seas controlled by a weakened surface halocline (Okazaki et al., 2010; Menviel et al., 2012; Gong et al., 2019). The intensified vertical convection transported warm and less saline surface water down to the intermediate depths (Gong et al., 2019). Owing to enhanced southward advection of the glacial NPIW into low-latitude Pacific (Max et al., 2017; Gong et al., 2019), the strengthened glacial NPIW formation in the subarctic Pacific possibly led to decline of baroclinic pressure gradient between the Pacific and the South China Sea.

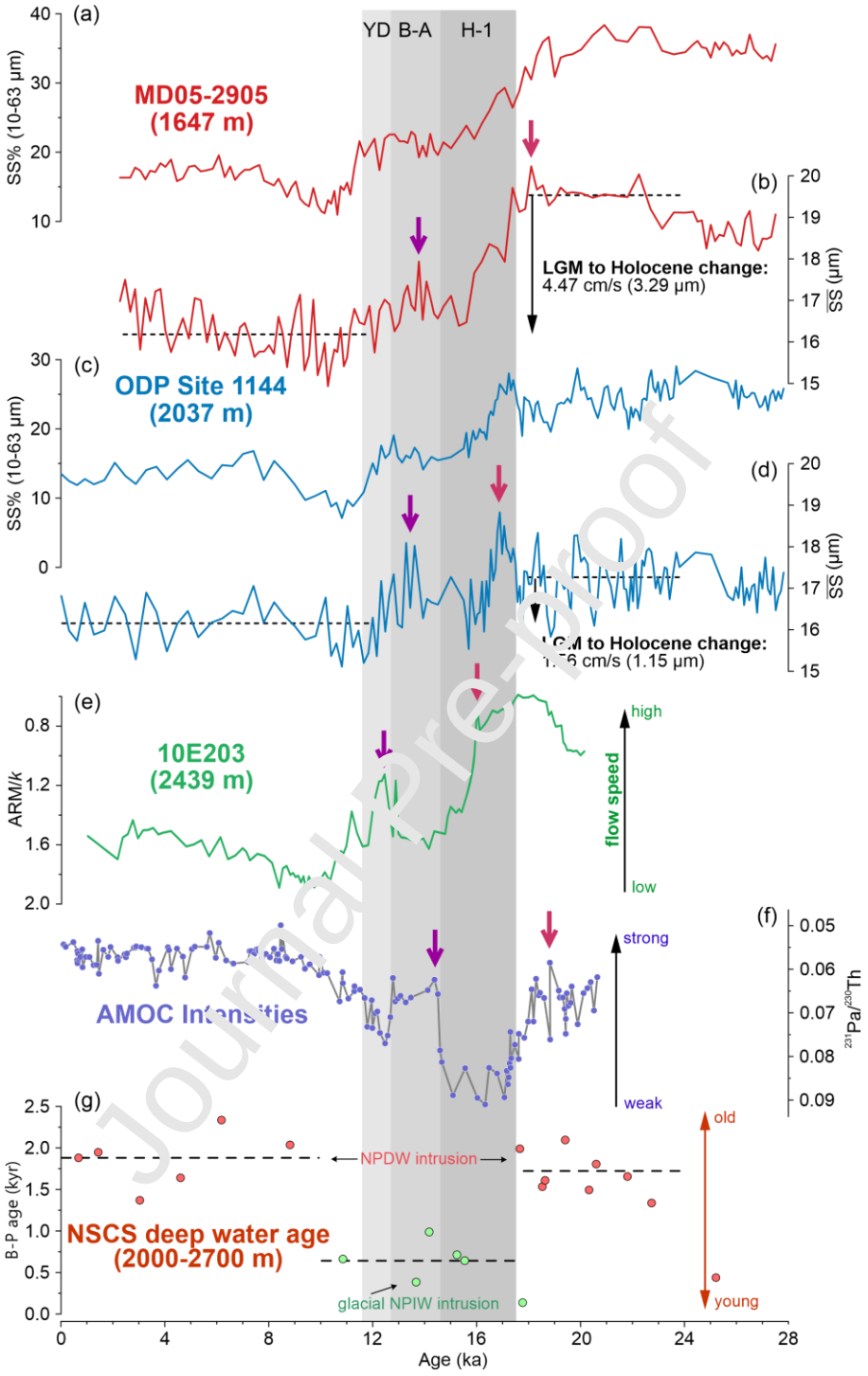

Figure 5. Temporal changes of SS% and $\overline{SS}$ in (a,b) Core MD05-2905 and (c,d) ODP Site 1144. The vertical arrows in (b) and (d) show the velocity differences between the LGM and the Holocene conditions. (e) the ratios between anhysteretic remnant magnetization (ARM) and magnetic susceptibility (k) in Core 10E203 at 2440 m (Zheng et al., 2016). (f) $^{231}Pa/^{230}Th$ records of the Bermuda Rise showing changes of the AMOC intensities (Lippold et al., 2019; McManus et al., 2004). (g) The age difference of benthic (B) and planktonic (P) foraminifers in the northern South China Sea indicating ages of deep water mass (Wan and Jian, 2014).

Increased intermediate water formation in the subarctic Pacific during the H-1 was regulated by slowdown of the Atlantic Meridional Overturning Circulation (AMOC) via teleconnection between the Atlantic and Pacific Oceans (Okazaki et al., 2010; Menviel et al., 2012; Gong et al., 2019). Onset of the H-1 *sensu stricto*, marked by massive deposition of ice-rafted detritus in the North Atlantic and collapse of the AMOC, was dated at ~17.5 ka (Hemming, 2004). However, initiation of slowdown of the AMOC and built-up of a subsurface heat reservoir in the subpolar Atlantic could be traced back to as early as ~18.8 ka (Figure 5f; McManus et al., 2004; Hall et al., 2006; Stanford et al., 2006, 2011; Max et al., 2022). Through the atmospheric teleconnection, slowdown of the AMOC led to immediate weakening of the surface halocline and increasing of NPIW formation in the subarctic Pacific (Wu et al., 2008; Okumura et al., 2009; Gong et al., 2019). Accordingly, the elevated glacial NPIW formation in the subarctic Pacific was possibly initialed as early as ~19 ka, which was in line with onset of the deep circulation slowdown in the South China Sea observed herein. Therefore, we propose that declining of current speeds in the deep South China Sea, indicated by decreasing $\overline{SS}$ and SS% values of Core MD05-2905 and ODP Site 1144, is caused by elevated intrusion of the glacial NPIW in response to weakening of the AMOC.

4.3. Gradual changes of current intensity towards deeper water

It is worth noting that the current speed decrease at Core MD05-2905 (~1647 m) commenced prior to that of ODP Site 1144 (~2037 m): the $\overline{SS}$ and SS% of Core MD05-2905 initialed to decrease at ~18.8–18.2 ka, while those of ODP Site 1144 initialed to decrease at ~17.2–16.9 ka (Figure 5a-d). Using the ratios between anhysteretic remnant magnetization (ARM) and magnetic susceptibility (k), Zheng et al (2016) reconstructed the variations of current intensities at ~2440 m water depth in the northern South China Sea (~120 km east of the studied

contourite drift), observing a decrease of deep-water current speed at ~16.0 ka (Figure 5e). Considering the water depth of the three cores, it seems that the onset of such deep current slowdown in the northern South China Sea starts earlier in relatively shallow water depth and develops gradually towards the deep portion. Zheng et al (2016) also observed a current intensification during the Younger Dryas (YD, 12.7–11.6 ka) cold event, peaked at ~12.3 ka (Figure 5e). Strengthening of the deep currents was also observed in the $\overline{SS}$ records of Core MD05-2905 and ODP Site 1144, respectively at ~13.8 ka in Core MD05-2905 and ~13.7–13.4 ka in ODP Site 1144. Combining the records of the three cores, we found that these current resumption events also occurred in chronological order from relatively shallow to deep water portions in the northern South China Sea.

As paleocurrent intensity in the South China Sea was regulated by the glacial NPIW intrusion during the last deglaciation, our results implied that impacts of the glacial NPIW on deep circulation in the South China Sea was probably a process extending gradually from relatively shallow to deep portions of the deep water mass. The glacial NPIW was a nutrient-depleted water mass overlying the NPDW, penetrating to as deep as ~2000 m (Keigwin, 1998; Matsumoto et al., 2002; Rae et al., 2020). Along with the slowdown of the AMOC starting at ~18.8 ka, the glacial NPIW formation in the subarctic Pacific was enhanced (Okazaki et al., 2010; Menviel et al., 2012; Gong et al., 2019). The water mass at the same depth range south of the subarctic Pacific was, however, still occupied by the NPDW, which was colder and denser. As a result, the glacial NPIW would gradually shoal in the course of southward advection, riding on the NPDW. As time elapsed, owing to continuous southward advection of the glacial NPIW and gradual water exchange between the two water masses, influence of the glacial NPIW extended slowly towards deeper portion in the North Pacific. Such mechanism can well explain

changes of the deep current intensity in the South China Sea. The 1600–1700 m depth started to be affected by the glacial NPIW at ~18.8–18.2 ka, almost coincide with onset of the AMOC slowdown (Figure 5a,b). Meanwhile, current intensities at 2000 to 2400 m maintained at the LGM level, as this depth range was still occupied by the NPDW. The current intensity at ~2000 m started to decrease from ~17.2–16.9 ka (Figure 5c,d), implying that the water mass above ~2000 m depth from the subarctic to subtropical Pacific was then all taken over by the glacial NPIW. This is well coincided with the intrusion of newly-formed young deep water into the >2000 m portion of South China Sea (Figure 5g; Wan and Jian, 2014). Interestingly, the glacial NPIW continued to exert its influence on the deep South China Sea circulation towards the >2000 m depth portion, and flow speed at ~2400 m has decreased since ~16 ka (Figure 5e, Zheng et al., 2016). It implies that the South China Sea deep water in the >2000 m portion was also gradually renewed by the glacial NPIW during the late phase of the H-1. Since the B-A warming at ~14.6 ka, the AMOC reinvigorated and thus development of the glacial NPIW was largely depressed, giving rise to reduced injection of low-salinity surface water to the intermediate depths in the subarctic Pacific (Knorr and Lohmann, 2003; Weaver et al., 2003; Ng et al., 2018). As a feedback to the elevated density gradient between the Pacific and the South China Sea at intermediate depths, a gradual increasing of paleocurrent speeds in the northern South China Sea was observed, spreading from ~1600–1700 m to ~2400 m in around 1.4 ka (13.7–12.3 ka) (Figure 5).

4.4. The effects of strengthened deep-sea currents on sediment deposition of the contourite drift

According to the arithmetic relation of $\overline{SS}$ with deep-sea current speeds established by McCave et al (2017), 1 μm change of $\overline{SS}$ represents 1.36 ± 0.19 cm/s (± 2σ error) change in current speeds. Therefore, the 3.29 μm difference between the LGM mean and the Holocene

mean values of the $\overline{SS}$ embodies a decrease of ~4.47 cm/s of deep-sea current speed at ~1650 m water depth (Core MD05-2905), while the 1.07 μm difference at ODP Site 1144 embodies a current speed decrease of ~1.56 cm/s at ~2000 m water depth (Figure 5b,d). At present, the mean current velocity on the elongated contourite drift at southeast off Dongsha Islands varies in the range of 0–2 cm/s (Zhao et al., 2015). Taking such values as the Holocene mean of the northern South China Sea, current speeds were roughly 1.5–3.5 cm/s at 2000 m and 4.5–6.5 cm/s at ~1650 m during the LGM, thus the latter was around 2–3 times as high as the former.

LSR of Core MD05-2905 and ODP Site 1144 is ~ 5 times higher than the average LSR of northern South China Sea for the Quaternary Period (~12 cm/kyr, Huang and Wang, 2006). During the last glacial period, LSR of ODP Site 1144 even reach ~ 10–20 times higher than the average value of northern South China Sea (Figure 2). The high LSR on the contourite drift implies that there are strong sediment focusing by "deep-sea storms", the repeated resuspension of sediments by short-lived strong current events (McCave and Hall, 2006). The elevated LSR of ODP Site 1144 during the last glacial period thus indicates that the ~1.5 cm/s increasing (relative to the Holocene mean) of the average value of deep-current velocity has largely increased the frequencies of the "deep sea storms" and enhanced sediment focusing by these events, though the mean-state of the current is below the threshold for selective deposition of sortable silts (10–15 cm/s; McCave and Hall, 2006). For Core MD05-2905, the LSR for the last glacial and the Holocene is at almost the same level (Figure 2), though the current velocities are much stronger during the last glacial period (~4.5 cm/s higher, Figure 5b). It can probably be explained by the balance between sediment focusing and sediment winnowing by strong currents. When the velocity of currents exceeds ~15 cm/s, part of the sediments is winnowed by the strong currents, causing decreases of sediment accumulation rates (McCave and Hall, 2006). The strong currents

at ~1650 m during the last glacial period, increased the probability of sediment focusing by "deep-sea storms" and also the probability of sediment winnowing by currents that is "too strong". As a result, though the sediments of the last glacial period are much coarser than those of the Holocene, the sedimentation rates are not obviously increased.

To summarize, we propose that deep-sea currents at ~2000 m depth was averagely ~1.5 cm/s stronger in the LGM than in the Holocene, probably because of the higher frequencies of "deep-sea storms" occurrence. The more frequent "deep-sea storms" lead to enhanced sediment focusing on the contourite drift and thus much higher LSR during the last glacial period. At ~1650 m depth, the difference between the LGM and the Holocene mean current velocities can reach as high as ~4.5 cm/s. Such a great increase of deep current velocity promoted the probability of sediment winnowing while enhancing sediment focusing, leading to coarser sediment deposition on the contourite drift but no higher LSR relative to the Holocene condition.

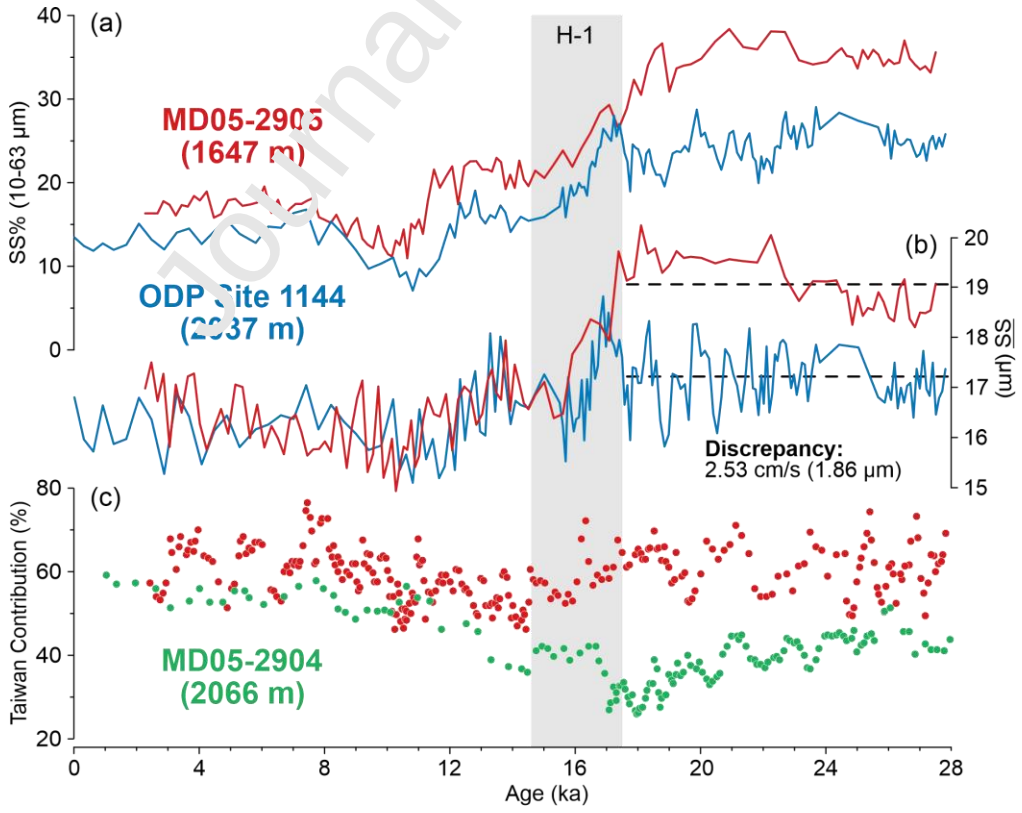

Figure 6. (a,b) Temporal changes of SS% and $\overline{SS}$ in Core MD05-2905 and ODP Site 1144 showing changes of stratification condition in the deep South China Sea at the onset of H-1. (c) fine-grained terrigenous contributions from Taiwan to Cores MD05-2904 and MD05-2905 (Liu et al., 2016).

4.5. Deep-water stratification of South China Sea since the last glacial period

Putting together the SS% and $\overline{SS}$ records of the two cores, it is clearly shown that: prior to the H-1, both SS% and $\overline{SS}$ are greater in Core MD05-2905 than in ODP Site 1144, while since onset of the H-1, approximate values and tendencies are presented in the two cores (Figure 6a,b). It suggests that current speeds are stronger at the relatively shallow than the deep portions of the deep South China Sea before occurrence of the H-1. The 1.86 ‰ discrepancy of $\overline{SS}$ between the two cores indicates that current speeds at ~1650 m is around 2.53 cm/s higher than those at ~2000 m water depth (Figure 6b). Such cross-depth velocity variations reflect the changes of stratification in the deep South China Sea in response to occurrence of the H-1. At present, diapycnal mixing in the deep South China Sea is around 2 orders of magnitude greater than its counterpart in the western Pacific, making deep water in the South China Sea more vertically homogenous than the western Pacific (Tian et al., 2009). Whilst, vertical mixing in the deep South China Sea was relatively inactive during the last glacial period (Wan and Jian, 2014). Such variance can be attributed to alteration of stratification condition in the deep South China Sea in response to hydrographic changes in the North Pacific. Prior to the H-1, the upper portion of the deep South China Sea (~1650 m) was occupied by the glacial NPIW, while the lower portion (~2000 m) was filled by the NPDW, thus a strong stratification was developed between the two water masses. Although the NPDW was colder and denser than the glacial NPIW, its volume transport entering the South China Sea was likely much lower than the glacial NPIW. As a result, the paleocurrent intensity at ~2000 m was weaker than ~1650 m (Figure 6). Gradual deepward penetration of the glacial NPIW started at ~18.8 ka led to an increased intrusion of the glacial

NPIW into the deep South China Sea, and till onset of the H-1 at ~17.5 ka, the above 2000 m portion of deep water was fully occupied by the glacial NPIW. Deep-water stratification between relatively shallow (~1650 m) and deep (~2000 m) portions thus faded away owing to the homogeneity of seawater. The changes of stratification in the deep South China Sea can also have a great impact on variations of sediment contribution from the Taiwanese rivers (Figure 6c, data from Liu et al., 2016), which are the primary sources of detrital sediments in the deep South China Sea. The strong stratification configuration prior to the H-1 acted as a barrier to water mixing, inhibiting the vertical exchanges of both energy and materials. As a result, detrital sediments from Taiwan were 10–20% lower at 2000–2100 m (Core MD05-2904) than ~1650 m (Core MD05-2905) in the northern South China Sea (Figure 6c, Liu et al., 2016). Since onset of the H-1, the enhanced vertical mixing of deep water mass was conducive to the downward delivery of suspended particles into the deep portion of the South China Sea, resulting in an increased contribution of Taiwan-derived sediments to marine cores at 2000–2100 m water depth (Figure 6c, Liu et al., 2016). Noteworthily, such strong vertical mixing in the deep South China Sea was not receded in the Holocene, although the development of the glacial NPIW ceased in the subarctic Pacific (Max et al., 2014). At present, strong diapycnal mixing in the deep South China Sea is caused by the intensive internal tides/waves and mesoscale eddy activities (Tian et al., 2009). If oceanographic conditions in the deep South China Sea was not greatly altered, such processes can also interpret the strong vertical mixing during the entire Holocene.

5. Conclusions

Based upon the ‘sortable silt’ proxy of paleocurrent intensity of two sediment cores taken in the northern South China Sea, temporal changes of paleocurrent intensities in the deep South China Sea since the last glacial period were reconstructed. These results provide new insights

into understanding the variation of intermediate and deep hydrography of the North Pacific under the glacial boundary conditions, especially the processes how the glacial NPIW affected the low-latitude Pacific. The main conclusions are:

(1) Paleocurrent speeds at both ~1650 m and ~2000 m in the South China Sea has undergone a three-stage evolution since ~28 ka: strong currents during the LGM, followed by a gradual decrease of current speeds during the last deglaciation, and relatively weak currents in the Holocene. The discrepancies of current speeds between the last glacial period and the Holocene reach ~4.5 cm/s at ~1650 m water depth, and ~1.5 cm/s at ~2000 m.

(2) Decreases of paleocurrent speeds during the last deglaciation reflect the intrusion of the glacial NPIW into the South China Sea in response to slowdown of the AMOC via teleconnection. Current speeds started to decrease ~18.8–18.2 ka at ~1650 m, while they started to decrease ~17.2–16.9 ka at ~2000 m. Paleocurrent reintensification during the B-A warming also occurred earlier in the upper, and later in the lower portions of the deep South China Sea. Such processes suggested that the impacts of the glacial NPIW on the subtropical Pacific was a gradual process extending from relatively shallow to deep water depths.

(3) A strong stratification existed in the deep South China Sea during the last glacial period, because the upper portion of deep water mass was occupied by the glacial NPIW, while the lower portion was occupied by the NPDW. Owing to the deepward extending influence of the glacial NPIW during the H-1, vertical mixing in the deep South China Sea was largely enhanced and stratification faded away.

Acknowledgments

This research used samples provided by the International Ocean Discovery Program (IODP). The staff in the Kochi Core Center (KCC) is appreciated for their assistance in sub-sampling ODP Site 1144. Crew and scientists on board of the 'MD147/Marco Polo-IMAGES XII' cruise of R/V Marion Dufresne and ODP Leg 184 are acknowledged for obtaining the sediment cores. Brian Romans and other two anonymous reviewers are acknowledged for their valuable and constructive comments. This work is financially funded by National Science Foundation of China (41776047).

Data Availability

The grain-size datasets of ODP Site 1144 and Core MD05-2905 are available as supplementary materials.

References

Bianchi, G.G., Hall, I.R., McCave, I.N., Joseph, L., 1999. Measurement of the sortable silt current speed proxy using the SediGraph 5100 and Coulter Multisizer IIe: precision and accuracy. Sedimentology 46, 1001–1014. https://doi.org/10.1046/j.1365-3091.1999.00256.x.

Broecker, W., Clark, E., Barker, S., 2008. Near constancy of the Pacific Ocean surface to mid-depth radiocarbon-age difference over the last 20 kyr. Earth Planet. Sci. Lett. 274, 322–326. https://doi.org/10.1016/j.epsl.2008.07.035.

Bühring, C., Sarnthein, M., Erlenkeuser, H., 2004. Toward a high-resolution stable isotope stratigraphy of the last 1.1 m.y.: Site 1144, South China Sea, in: Prell, W.L., Wang, P., Blum, P., Rea, D.K., Clemens, S.C. (Eds.), Proceedings of the Ocean Drilling Program,

Scientific Results, Volume 184. Ocean Drilling Program, College Station, pp. 1–29. https://doi.org/10.2973/odp.proc.sr.184.205.2004.

Coakley, J.P., Syvitski, J.P.M., 1991. SediGraph technique, in: Syvitski, J.P.M. (Ed.), Principles, Methods, and Application of Particle Size Analysis. Cambridge University Press, Cambridge, pp. 129–142. https://doi.org/10.1017/CBO9780511626142.013.

Culp, J., Parent, A.M., Abolfazli, E., Strom, K., and Romans, B.W., 2021. Advective sorting of silt by currents: A laboratory study. Sedimentology 68, 3116–3140. https://onlinelibrary.wiley.com/doi/10.1111/sed.12889.

Du, S., Xiang, R., Liu, J., Liu, J.P., Ariful Islam, G.M., Chen, M., 2020. The present-day atmospheric dust deposition process in the South China Sea. Atmos. Environ. 223, 117261. https://doi.org/10.1016/j.atmosenv.2020.117261.

Duce, R.A., Liss, P.S., Merrill, J.T., Atlas, E.L., Buat-Menard, P., Hicks, B.B., Miller, J.M., Prospero, J.M., Arimoto, R., Church, T.M., Ellis, W., Galloway, J.N., Hansen, L., Jickells, T.D., Knap, A.H., Reinhardt, K.H., Schneider, B., Soudine, A., Tokos, J.J., Tsunogai, S., Wollast, R., Zhou, M., 1991. The atmospheric input of trace species to the world ocean. Global Biogeochem. Cycles 5, 193–259. https://doi.org/10.1029/91GB01778.

Galbraith, E.D., Jaccard, S.L., Pedersen, T.F., Sigman, D.M., Haug, G.H., Cook, M., Southon, J.R., Francois, R., 2007. Carbon dioxide release from the North Pacific abyss during the last deglaciation. Nature 449, 890–893. https://doi.org/10.1038/nature06227.

Gong, X., Lembke-Jene, L., Lohmann, G., Knorr, G., Tiedemann, R., Shi, X., 2019. Enhanced North Pacific deep-ocean stratification by stronger intermediate water formation during Heinrich Stadial 1. Nat. Commun. 10, 656. https://doi.org/10.1038/s41467-019-08606-2.

Gray, W.R., Rae, J.W.B., Wills, R.C.J., Shevenell, A.E., Taylor, B., Burke, A., Foster, G.L., Lear, C.H., 2018. Deglacial upwelling, productivity and CO_2 outgassing in the North Pacific Ocean. Nat. Geosci. 11, 340–344. https://doi.org/10.1038/s41561-018-0108-6.

Hall, I.R., Moran, S.B., Zahn, R., Knutz, P.C., Shen, C.-C., Edwards, R.L., 2006. Accelerated drawdown of meridional overturning in the late-glacial Atlantic triggered by transient pre-H event freshwater perturbation. Geophys. Res. Lett. 33, L16616. https://doi.org/10.1029/2006GL026239.

Heaton, T.J., Köhler, P., Butzin, M., Bard, E., Reimer, R.W., Austin, W.E.N., Ramsey, C.B., Grootes, P.M., Hughen, K.A., Kromer, B., Reimer, P., Adkins, J., Burke, A., Olsen, J., Skinner, L.C., 2020. Marine20—the marine radiocarbon age calibration curve (0–55,000 cal BP). Radiocarbon 62, 779–820. https://doi.org/10.1017/RDC.2020.68.

Hemming, S.R., 2004. Heinrich events: massive Late Pleistocene detritus layers of the North Atlantic and their global imprint. Rev. Geophys. 42, 1–43. https://doi.org/10.1029/2003RG000128.

Herguera, J.C., Herbert, T., Kashgarian, M., Charles, C., 2010. Intermediate and deep water mass distribution in the Pacific during the Last Glacial Maximum inferred from oxygen and carbon stable isotopes. Quat. Sci. Rev. 29, 1228–1245. https://doi.org/10.1016/j.quascirev.2010.02.009.

Horikawa, K., Asahara, Y., Yamamoto, K., Okazaki, Y., 2010. Intermediate water formation in the Bering Sea during glacial periods: Evidence from neodymium isotope ratios. Geology 38, 435–438. https://doi.org/10.1130/G30225.1.

Hu, D., Böning, P., Köhler, C.M., Hillier, S., Pressling, N., Wan, S., Brumsack, H.-J., Clift, P.D., 2012. Deep sea records of the continental weathering and erosion response to East Asian

monsoon intensification since 14 ka in the South China Sea. Chem. Geol. 326–327, 1–18. https://doi.org/10.1016/j.chemgeo.2012.07.024.

Huang, W., Wang, P., 2006. Sediment mass and distribution in the South China Sea since the Oligocene. Sci. China Ser. D-Earth Sci. 49, 1147–1155. https://doi.org/10.1007/s11430-006-2019-4.

Jaccard, S.L., Galbraith, E.D., 2013. Direct ventilation of the North Pacific did not reach the deep ocean during the last deglaciation. Geophys. Res. Lett. 40, 199–203. https://doi.org/10.1029/2012GL054118.

Keigwin, L.D., 1998. Glacial age hydrography of the far northwest Pacific Ocean. Paleoceanography 13, 323–339. https://doi.org/10.1029/98PA00874.

Kienast, M., Higginson, M.J., Mollenhauer, G., Eglinton, T.I., Chen, M.-T., Calvert, S.E., 2005. On the sedimentological origin of down-core variations of bulk sedimentary nitrogen isotope ratios. Paleoceanography 20, PA2009. https://doi.org/10.1029/2004PA001081.

Kissel, C., Laj, C., Jian, Z., Wang, P., Vandres, C., Rebolledo-Vieyra, M., 2020. Past environmental and circulation changes in the South China Sea: Input from the magnetic properties of deep-sea sediments. Quat. Sci. Rev. 236, 106263. https://doi.org/10.1016/j.quascirev.2020.106263.

Knorr, G., Lohmann, G., 2003. Southern Ocean origin for the resumption of Atlantic thermohaline circulation during deglaciation. Nature 424, 532–536. https://doi.org/10.1038/nature01855.

Laj, C., Wang, P., Balut, Y., 2005. Les rapports de campagnes à la mer MD 147/MARCO POLO-IMAGES XII à bord du “Marion Dufresne”. Institut Polaire Français, Plouzané.

Lambeck, K., Rouby, H., Purcell, A., Sun, Y., Sambridge, M., 2014. Sea level and global ice volumes from the Last Glacial Maximum to the Holocene. Proc. Natl. Acad. Sci. 111, 15296–15303. https://doi.org/10.1073/pnas.1411762111.

Lan, J., Zhang, N., Wang, Y., 2013. On the dynamics of the South China Sea deep circulation. J. Geophys. Res. Oceans 118, 1206–1210. https://doi.org/10.1002/jgrc.20104.

Li, G., Rashid, H., Zhong, L., Xu, X., Yan, W., Chen, Z., 2018. Changes in deep water oxygenation of the South China Sea since the last glacial period. Geophys. Res. Lett. 45, 9058–9066. https://doi.org/10.1029/2018GL078568.

Li, L., Qu, T., 2006. Thermohaline circulation in the deep South China Sea basin inferred from oxygen distributions. J. Geophys. Res. Oceans 111, C05017. https://doi.org/10.1029/2005JC003164.

Lippold, J., Pöppelmeier, F., Süfke, F., Gutjahr, M., Goepfert, T.J., Blaser, P., Friedrich, O., Link, J.M., Wacker, L., Rheinberger, S., Jaccard S.L., 2019. Constraining the variability of the Atlantic Meridional Overturning Circulation during the Holocene. Geophys. Res. Lett. 46, 11338–11346. https://doi.org/10.1029/2019GL084988.

Liu, Z., Huang, W., Li, J., Wang, P., Wang, R., Yu, K., Zhao, J., 2009. Sedimentology, in: Wang, P., Li, Q. (Eds.), The South China Sea: Paleoceanography and Sedimentology. Springer, Dordrecht, pp. 171–295. https://doi.org/10.1007/978-1-4020-9745-4_4.

Liu, Z., Colin, C., Li, X., Zhao, Y., Tuo, S., Chen, Z., Siringan, F.P., Liu, J.T., Huang, C.-Y., You, C.-F., Huang, K.-F., 2010. Clay mineral distribution in surface sediments of the northeastern South China Sea and surrounding fluvial drainage basins: Source and transport. Mar. Geol. 277, 48–60. https://doi.org/10.1016/j.margeo.2010.08.010.

Liu, Z., Zhao, Y., Colin, C., Stattegger, K., Wiesner, M.G., Huh, C.-A., Zhang, Y., Li, X., Sompongchaiyakul, P., You, C.-F., Huang, C.-Y., Liu, J.T., Siringan, F.P., Le, K.P., Sathiamurthy, E., Hantoro, W.S., Liu, J., Tuo, S., Zhao, S., Zhou, S., He, Z., Wang, Y., Bunsomboonsakul, S., Li, Y., 2016. Source-to-sink transport processes of fluvial sediments in the South China Sea. Earth-Sci. Rev. 153, 238–273. https://doi.org/10.1016/j.earscirev.2015.08.005.

Matsumoto, K., Oba, T., Lynch-Stieglitz, J., Yamamoto, H., 2002. Interior hydrography and circulation of the glacial Pacific Ocean. Quat. Sci. Rev. 21, 1693–1704. https://doi.org/10.1016/S0277-3791(01)00142-1.

Max, L., Lembke-Jene, L., Riethdorf, J.-R., Tiedemann, R., Nürnberg, D., Kühn, H., Mackensen, A., 2014. Pulses of enhanced North Pacific Intermediate Water ventilation from the Okhotsk Sea and Bering Sea during the last deglaciation. Clim. Past 10, 591–605. https://doi.org/10.5194/cp-10-591-2014.

Max, L., Nürnberg, D., Chiessi, C.M., Lenz, M.M., Mulitza, S., 2022. Subsurface ocean warming preceded Heinrich Events. Nat. Commun. 13, 4217. https://doi.org/10.1038/s41467-022-31754-x.

Max, L., Rippert, N., Lembke-Jene, L., Mackensen, A., Nürnberg, D., Tiedemann, R., 2017. Evidence for enhanced convection of North Pacific Intermediate Water to the low-latitude Pacific under glacial conditions. Paleoceanography 32, 41–55. https://doi.org/10.1002/2016PA002994.

McCave, I.N., Andrews, J.T., 2019. Distinguishing current effects in sediments delivered to the ocean by ice. I. Principles, methods and examples. Quat. Sci. Rev. 212, 92–107. https://doi.org/10.1016/j.quascirev.2019.03.031.

McCave, I.N., Hall, I.R., 2006. Size sorting in marine muds: Processes, pitfalls, and prospects for paleoflow-speed proxies. Geochem. Geophys. Geosyst. 7, Q10N05. https://doi.org/10.1029/2006GC001284.

McCave, I.N., Hall, I.R., Bianchi, G.G., 2006. Laser vs. settling velocity differences in silt grainsize measurements: estimation of palaeocurrent vigour. Sedimentology 53, 919–928. https://doi.org/10.1111/j.1365-3091.2006.00783.x.

McCave, I.N., Manighetti, B., Robinson, S.G., 1995. Sortable silt and fine sediment size/composition slicing: parameters for palaeocurrent speed and palaeoceanography. Paleoceanography 10, 593–610. https://doi.org/10.1029/94PA03039.

McCave, I.N., Thornalley, D.J.R., Hall, I.R., 2017. Relation of sortable silt grain-size to deep-sea current speeds: Calibration of the 'Mud Current Meter'. Deep-Sea Res. Part I 127, 1–12. http://dx.doi.org/10.1016/j.dsr.2017.07.003.

McManus, J.F., Francois, R., Gherardi, J. M., Keigwin, L.D., Brown-Leger, S., 2004. Collapse and rapid resumption of Atlantic meridional circulation linked to deglacial climate changes. Nature 428, 834–837. https://doi.org/10.1038/nature02494.

Menviel, L., Timmermann, A., Elison Timm, O., Mouchet, A, 2011. Deconstructing the Last Glacial Termination: The role of millennial and orbital-scale forcings. Quat. Sci. Rev. 30, 1155–1172. https://doi.org/10.1016/j.quascirev.2011.02.005.

Menviel, L., Timmermann, A., Elison Timm, O., Mouchet, A., Abe-Ouchi, A., Chikamoto, M.O., Harada, N., Ohgaito, R., Okazaki, Y., 2012. Removing the North Pacific halocline: Effects on global climate, ocean circulation and the carbon cycle. Deep-Sea Res. Part II 61–64, 106–113. https://doi.org/10.1016/j.dsr2.2011.03.005.

Ng, H.C., Robinson, L.F., McManus, J.F., Mohamed, K.J., Jacobel, A.W., Ivanovic, R.F., Gregoire, L.J., Chen, T., 2018. Coherent deglacial changes in western Atlantic Ocean circulation. Nat. Commun. 9, 2947. https://doi.org/10.1038/s41467-018-05312-3.

Ohkushi, K.I., Itaki, T., Nemoto, N., 2003. Last glacial–Holocene change in intermediate-water ventilation in the Northwestern Pacific. Quat. Sci. Rev. 22, 1477–1484. https://doi.org/10.1016/S0277-3791(03)00082-9.

Okazaki, Y., Sagawa, T., Asahi, H., Horikawa, K., Onodera, J., 2012. Ventilation changes in the western North Pacific since the last glacial period. Clim. Past 8, 17–24. https://doi.org/10.5194/cp-8-17-2012.

Okazaki, Y., Timmermann, A., Menviel, L., Harada, N., Abe-Ouchi, A., Chikamoto, M., Mouchet, A., Asahi, H., 2010. Deep water formation in the North Pacific during the last glacial termination. Science 329, 200–204. https://doi.org/10.1126/science.1190612.

Okumura, Y.M., Deser, C., Hu, A., Timmermann, A., Xie, S.-P., 2009. North Pacific climate response to freshwater forcing in the subarctic North Atlantic: oceanic and atmospheric pathways. J. Clim. 22, 1424–1445. https://doi.org/10.1175/2008JCLI2511.1.

Qu, T., Girton, J.B., Whitehead, J.A., 2006. Deepwater overflow through Luzon Strait. J. Geophys. Res. Oceans 111, C01002. https://doi.org/10.1029/2005JC003139.

Rae, J.W.B., Gray, W.R., Wills, R.C.J., Eisenman, I., Fitzhugh, B., Fotheringham, M., Littley, E.F.M., Ridgwell, A., Taylor, B., Burke, A., 2020. Overturning circulation, nutrient limitation, and warming in the Glacial North Pacific. Sci. Adv. 6, eabd1654. https://doi.org/10.1126/sciadv.abd1654.

Rella, S.F., Tada, R., Nagashima, K., Ikehara, M., Itaki, T., Ohkushi, K.I., Sakamoto, T., Harada, N., Uchida, M., 2012. Abrupt changes of intermediate water properties on the northeastern

slope of the Bering Sea during the last glacial and deglacial period. Paleoceanography 27, PA3203. https://doi.org/10.1029/2011PA002205.

Shao, L., Li, X., Geng, J., Pang, X., Lei, Y., Qiao, P., Wang, L., Wang, H., 2007. Deep water bottom current deposition in the northern South China Sea. Sci. China Ser. D-Earth Sci. 50, 1060–1066. https://doi.org/10.1007/s11430-007-0015-y.

Southon, J., Kashgarian, M., Fontugne, M., Metivier, B., Yim, W.W.-S., 2002. Marine reservoir corrections for the Indian Ocean and Southeast Asia. Radiocarbon 44, 167–180. https://doi.org/10.1017/S0033822200064778.

Stanford, J.D., Rohling, E.J., Hunter, S.E., Roberts, A.P., Rasmussen, S.O., Bard, E., McManus, J., Fairbanks, R.G., 2006. Timing of mwp-1a and climate responses to meltwater injections. Paleoceanography 21, PA4103. https://doi.org/10.1029/2006PA001340.

Stanford, J.D., Rohling, E.J., Bacon, S., Roberts, A.P., Grousset, F.E., Bolshaw, M., 2011. A new concept for the paleoceanographic evolution of Heinrich event 1 in the North Atlantic. Quat. Sci. Rev. 30, 1047–1066. https://doi.org/10.1016/j.quascirev.2011.02.003.

Stuiver, M., Reimer, P. J., 1993. Extended ^{14}C data base and revised CALIB 3.0 ^{14}C age calibration program. Radiocarbon 35, 215–230. https://doi.org/10.1017/S0033822200013904

Sun, X., Luo, Y., Huang, F., Tian, J., Wang, P., 2003. Deep-sea pollen from the South China Sea: Pleistocene indicators of East Asian monsoon. Mar. Geol. 201, 97–118. https://doi.org/10.1016/S0025-3227(03)00211-1.

Tamburini, F., Adatte, T., Föllmi, K., Bernasconi, S.M., Steinmann, P., 2003. Investigating the history of East Asian monsoon and climate during the last glacial–interglacial period (0–

140 000 years): mineralogy and geochemistry of ODP Sites 1143 and 1144, South China Sea. Mar. Geol. 201, 147–168. https://doi.org/10.1016/S0025-3227(03)00214-7.

Tian, J., Yang, Q., Zhao, W., 2009. Enhanced diapycnal mixing in the South China Sea. J. Phys. Oceanogr. 39, 3191–3203. https://doi.org/10.1175/2009JPO3899.1.

Wan, S., Jian, Z., 2014. Deep water exchanges between the South China Sea and the Pacific since the last glacial period. Paleoceanography 29, 1162–1178. https://doi.org/10.1002/2013PA002578.

Wan, S., Jian, Z., Dang, H., 2018. Deep hydrography of the South China Sea and deep water circulation in the Pacific since the last glacial maximum. Geochem. Geophys. Geosyst. 19, 1447–1463. https://doi.org/10.1029/2017GC007377.

Wang, L., Sarnthein, M., Erlenkeuser, H., Grimalt, J., Grootes, P., Heilig, S., Ivanova, E., Kienast, M., Pelejero, C., Pflaumann, U., 1999. East Asian monsoon climate during the late Pleistocene: high-resolution sediment records from the South China Sea. Mar. Geol. 156, 245–284. https://doi.org/10.1016/S0025-3227(98)00182-0.

Wang, P., Prell, W.L., Blum, P., shipboard scientists, 2000. Proceedings of the Ocean Drilling Program, Initial Reports, Volume 184. Ocean Drilling Program, College Station. https://doi.org/10.2973/odp.proc.ir.184.2000.

Wang, S.-H., Hsu, N.C., Tsay, S.-C., Lin, N.-H., Sayer, A.M., Huang, S.-J., Lau, W.K.M., 2012. Can Asian dust trigger phytoplankton blooms in the oligotrophic northern South China Sea? Geophys. Res. Lett. 39, L05811. https://doi:10.1029/2011GL050415.

Weaver, A.J., Saenko, O.A., Clark, P.U., Mitrovica, J.X., 2003. Meltwater pulse 1A from Antarctica as a trigger of the Bølling-Allerød warm interval. Science 299, 1709–1713. https://doi.org/10.1126/science.1081002.

Wei, G., Liu, Y., Li, X., Shao, L., Fang, D., 2004. Major and trace element variations of the sediments at ODP Site 1144, South China Sea, during the last 230 ka and their paleoclimate implications. Palaeogeogr. Palaeoclimatol. Palaeoecol. 212, 331–342. https://doi.org/10.1016/j.palaeo.2004.06.011.

Wu, L., Li, C., Yang, C., Xie, S.-P., 2008. Global teleconnections in response to a shutdown of the Atlantic meridional overturning circulation. J. Clim. 21, 3002–3019. https://doi.org/10.1175/2007JCLI1858.1.

Wu, Q., Colin, C., Liu, Z., Douville, E., Dubois-Dauphin, Q., Frank, N., 2015. New insights into hydrological exchange between the South China Sea and the western Pacific Ocean based on the Nd isotopic composition of seawater. Deep-Sea Res. Part II 122, 25–40. https://doi.org/10.1016/j.dsr2.2015.11.005.

Yang, W., 2008. High-resolution sedimentary records since the last glacial in the northern South China Sea and its paleoclimatic evolution.: Tongji University, Shanghai. (*in Chinese with English abstract*). https://doi.org/10.7666/d.y1450025.

Yin, S., Hernández-Molina, F.J., Zhang, W., Li, J., Wang, L., Ding, W., Ding, W., 2019. The influence of oceanographic processes on contourite features: A multidisciplinary study of the northern South China Sea. Mar. Geol. 415, 105967. https://doi.org/10.1016/j.margeo.2019.105967.

Yoneda, M., Uno. H., Shibata, Y., Suzuki, R., Kumamoto, Y., Yoshida, K., Sasaki, T., Suzuki, A., Kawahata, H., 2007. Radiocarbon marine reservoir ages in the western Pacific estimated by pre-bomb molluscan shells. Nucl. Instrum. Methods Phys. Res. B 259, 432–437. https://doi.org/10.1016/j.nimb.2007.01.184.

Zhao, Y., Liu, Z., Zhang, Y., Li, J., Wang, M., Wang, W., Xu, J., 2015. In situ observation of contour currents in the northern South China Sea: Applications for deepwater sediment transport. Earth Planet. Sci. Lett. 430, 477–485. https://doi.org/10.1016/j.epsl.2015.09.008.

Zheng, X., Kao, S.-J., Chen, Z., Menviel, L., Chen, H., Du. Y., Wan, S., Yan, H., Liu, Z., Zheng, L., Wang, S., Li, D., Zhang, X., 2016. Deepwater circulation variation in the South China Sea since the Last Glacial Maximum. Geophys. Res. Lett. 43, 8590–8599. https://doi.org/10.1002/2016GL070342.

Zhu, Y., Sun, J., Wang, Y., Wei, Z., Yang, D., Qu, T., 2017. Effect of potential vorticity flux on the circulation in the South China Sea. J. Geophys. Res. Oceans 122, 6454–6469. https://doi.org/10.1002/2016JC012375.

Zhu, Y., Sun, J., Wang, W., Li, S., Xu, T., Wei, Z., Qu, T., 2019. Overview of the multi-layer circulation in the South China Sea. Prog. Oceanogr. 175, 171–182. https://doi.org/10.1016/j.pocean.2019.04.001.

Declaration of interests

The authors declare that they have no known competing financial interests or personal relationships that could have appeared to influence the work reported in this paper.

Highlights:

- Slowdown of SCS deep circulation in response to intrusion of the glacial NPIW
- Gradual deepward extending of the glacial NPIW in the subtropical Pacific
- Strong glacial stratification in the deep SCS vanished at onset of the H-1 Event